

Greedy Sensor Placement with Cost Constraints

Emily Clark, Travis Askham, Steven L. Brunton, *Member, IEEE*, J. Nathan Kutz, *Member, IEEE*

Abstract—The problem of optimally placing sensors under a cost constraint arises naturally in the design of industrial and commercial products, as well as in scientific experiments. We consider a relaxation of the full optimization formulation of this problem and then extend a well-established QR-based greedy algorithm for the optimal sensor placement problem without cost constraints. We demonstrate the effectiveness of this algorithm on data sets related to facial recognition, climate science, and fluid mechanics. This algorithm is scalable and often identifies sparse sensors with near optimal reconstruction performance, while dramatically reducing the overall cost of the sensors. We find that the cost-error landscape varies by application, with intuitive connections to the underlying physics. Additionally, we include experiments for various pre-processing techniques and find that a popular technique based on the singular value decomposition is often sub-optimal.

I. INTRODUCTION

THE problem of determining the optimal placement of sensors under a cost constraint is relevant to many fields of scientific research and industry. Indeed, such considerations are critical in evaluating global monitoring systems and characterizing spatio-temporal dynamics (e.g. the brain, ocean and atmospheric dynamics, power grid networks, fluid flows, etc). For these applications, it is typical that only a limited number of measurements can be made of the system due to either prohibitive expense (i.e. either sensors are expensive, or they are expensive to place, or both) or the inability to place a sensor in a desired location (inaccessibility). Regardless, the goal of accurately reconstructing the state of the system from a limited number of measurements remains unchanged. To this end, we develop a principled, greedy sampling strategy whereby the sensor placement optimization is formulated as a cost-constrained problem in a relaxed form. We further introduce a parameter representing the balance between the quality of the reconstruction and the cost, and thus can evaluate explicitly the cost-error curve. The simple algorithmic structure proposed, which relies on a modification of the pivoted QR decomposition, provides an effective and scalable strategy for economical sensor placement for a wide range of scientific and engineering applications.

There is a significant body of literature on the subject of signal reconstruction from a limited number of point measurements (i.e. sensors). We do not seek to review this literature here, but point to [1]–[8] for a sense of the depth and diversity of the existing mathematical optimization formulations. The

related problem of controlling a system based on a limited number of measurements and actuators has also been well-studied. See, inter alia, [9]–[12]. The critical extension of these techniques considered here involves the consideration of the actual expense of the sensors and the cost of their placement, thus shaping a cost landscape that must be considered in order to more accurately assess the sensor placements.

In principle, the map from the measurements of a system to the full-state reconstruction can take any form. However, in this manuscript, we view sensor placement as an interpolation problem, i.e., given the values of a sample of some system at its interpolation points (sensors), we would like to approximately reconstruct the full state by applying a *linear* map to these values. There are a few reasons we limit ourselves to reconstruction based on a linear map: (i) it is easy to check the stability and optimality of a given set of points, (ii) it is straightforward to design efficient algorithms for sensor placement, and, (iii) as noted above, it is easy to interpret the sensor locations as mathematical objects, i.e. they are interpolation points.

Once the map is restricted to be linear, the goal is then to find sensor locations which give an accurate full-state approximation and result in a stable interpolation map. Of course, a brute-force solution of this problem may be obtained by searching over all possible subsets of the sensors but this approach quickly becomes intractable, as the number of subsets increases combinatorially. We must then seek efficient methods for finding nearly-optimal interpolation points. The efficient computation of such points given samples of the system has a rich history and has been considered in a variety of contexts. We will quickly review some of the dominant themes of the algorithms for selecting interpolation points.

Randomly placed sensors perform surprisingly well. For instance, Wright et al. observed that, given a generic basis in which samples of the signal will be sparse, it is possible to reconstruct a signal which has been downsampled or randomly projected [1]. The compressed sensing literature provides a theoretical basis for the surprising effectiveness of random, or rather *incoherent*, measurements in this setting; see, inter alia, [13]–[17]. We note that such an approach does not necessarily make use of any full-state observations of the system (though some model for the system is implied) and random sensors have been observed to be less efficient than sensors which take this data into account [8].

A common data-driven approach is to start with a *tailored basis* derived from the observed samples, typically given by the dominant singular vectors [18]–[21]. See [22], [23] for early examples of signal reconstruction from a limited number of sensors using such a basis. Of course, random sensors may still be used with tailored bases, but better accuracy and stability are possible with sensors chosen for the given basis.

E. Clark is with the Department of Physics at the University of Washington, Seattle, WA, 98195-1560 USA email: eclark7@uw.edu

S. Brunton is with the Department of Mechanical Engineering at the University of Washington, Seattle, WA, 98195-2600 USA email: sbrunton@uw.edu

T. Askham and J. N. Kutz are with the Department of Applied Mathematics at the University of Washington, Seattle, WA, 98195-3925 USA email: askham@uw.edu and kutz@uw.edu

A number of heuristic choices for the locations have been developed, including placing sensors at the extrema of the singular vectors [5]–[7].

Before we review some of the more principled data-driven sensor selection algorithms, we require some notation. For an index set J and any matrix \mathbf{M} , let $\mathbf{M}_{\cdot J}$ denote the matrix formed by the columns of \mathbf{M} with index in J . Let our samples of data be arranged in the rows of a matrix \mathbf{X} and let Ψ be some matrix derived from \mathbf{X} (e.g. Ψ may be taken to be the right singular vectors of \mathbf{X} , random linear combinations of the rows of \mathbf{X} , or \mathbf{X} itself). If the size of J is fixed, it is known that the set of indices \hat{J} which maximizes the product of the singular values of $\Psi_{\cdot J}$ provides optimal interpolation points for Ψ [24], [25] (see Theorem 1 below for the definition of optimal).

The problem of finding such a \hat{J} is nonconvex and NP-hard, but there are reasonable approximate algorithms. Gu and Eisenstat developed a polynomial time algorithm for computing J when the optimality criterion is relaxed slightly [24]. Joshi and Boyd formulated sensor placement as an approximate convex problem, which may be solved in polynomial time and is observed to provide nearly optimal sensors [2]. While both of these approaches scale polynomially in the number of sensors and the size of the data, they are not as computationally efficient as some of the existing greedy algorithms for interpolation, especially for high-dimensional data. Further, the examples on which the greedy algorithms are known to fail appear to be pathological, i.e. it is incredibly unlikely that the greedy approach will fail in practice.

The greedy sensor selection algorithm which is of greatest interest in this manuscript is based on the column pivoted QR decomposition. In particular, for a given number of sensors k , one simply selects J to be the first k column pivots of Ψ (see Section II for an explanation as to why this is a greedy approach for maximizing the product of the singular values of $\Psi_{\cdot J}$). This algorithm is the basis for practical approaches to computing the interpolative decomposition [25], [26], which is commonly used to compress low-rank matrices. The algorithm is also used in the discrete empirical interpolation method (DEIM) from reduced order modeling [27], [28], in its more stable Q-DEIM formulation [29]. For high dimensional problems with many samples of data, standard techniques from the burgeoning field of randomized algorithms for linear algebra may be used to improve the efficiency of these schemes [30], [31].

In the sensor placement techniques described above, an optimal map and set of sensor locations are found for a fixed number of sensors. This is equivalent to the cost-constrained sensor placement problem when each sensor has the same cost. In the case that some sensor locations should be entirely excluded, corresponding to an infinite cost, i.e. an inaccessible measurement location, and the remaining locations are of uniform cost, again the algorithms above may be used by simply narrowing the search to the allowed sensor locations (note that such a restriction has implications for the stability of the interpolation map).

We show that it is simple to modify the pivoted QR based scheme to incorporate a cost constraint for problems

in between these extremes, i.e. for problems in which some sensor locations cost more than others but may be more informative. The method is obtained by writing the cost-constrained problem in a relaxed form, which introduces a parameter representing the balance between the quality of the reconstruction and the cost, and then varying that parameter to trace out a cost-error curve. For each value of the parameter, we use a greedy algorithm to add sensor locations one-by-one.

We test the performance of our methods on data sets from facial recognition, climate science, and fluid mechanics using a standard training set/testing set apparatus. For some data sets, the proposed algorithm displays a significant advantage over methods based on randomly selected sensors. We also compare with known performance bounds and brute-force answers when possible and find that our algorithm is often near the optimal solution.

The remainder of this paper is organized as follows. In Section II, we summarize some relevant results from the interpolation literature and present our problem formulation. We then develop an algorithm for sensor placement in Section III which is a simple extension of the existing methods. We include a brief discussion of the effect of data pre-processing (i.e. the choice of Ψ) on the quality of the sensor locations in Section IV; in particular, we compare the performance when applied to the raw data, the first several singular vectors of the data, and randomized projections of the data. We then apply our methods to three data sets and discuss the performance in Section V. Finally, we provide some concluding remarks and indicate possible future avenues for research in Section VI.

II. PRELIMINARIES AND PROBLEM FORMULATION

In this section, we fix some notation, formulate the linear sensor placement problem with non-uniform cost constraints, and review some of the literature on the standard linear sensor placement problem with uniform cost.

A. Setting, notation, and problem formulation

Let $\mathbf{x}^i \in \mathbb{R}^n$ denote samples of some system and let $\boldsymbol{\eta} \in \mathbb{R}_+^n$ denote non-negative costs associated with each sample location. We collect the samples \mathbf{x}^i as the rows of a matrix $\mathbf{X} \in \mathbb{R}^{m \times n}$. The sensor placement problem with cost constraints then seeks out an optimal subset \hat{J} of the column indices of \mathbf{X} which balances the associated cost $\sum_{j \in \hat{J}} \eta_j$ with reconstruction error and stability, which we define below.

For a given set of indices, $J = \{j_1, \dots, j_l\}$, it is simple to construct the optimal linear map for reconstructing the entries in \mathbf{X} . Let

$$\hat{\mathbf{T}}(J) = \arg \min_{\mathbf{T} \in \mathbb{R}^{l \times n}} \|\mathbf{X} - \mathbf{X}_{\cdot J} \mathbf{T}\|_F, \quad (1)$$

where $\mathbf{X}_{\cdot J}$ denotes the matrix given by collecting the columns of \mathbf{X} whose indices are in J and $\|\cdot\|_F$ denotes the Frobenius norm. It is well known that $\hat{\mathbf{T}}(J) = \mathbf{X}_{\cdot J}^\dagger \mathbf{X}$, where $\mathbf{X}_{\cdot J}^\dagger$ denotes the Moore-Penrose pseudoinverse of $\mathbf{X}_{\cdot J}$, i.e. this is the least-squares solution. Therefore, the relative reconstruction error for linear sensor placement is given by

$$e(J) = \frac{\|\mathbf{X} - \mathbf{X}_{\cdot J} \mathbf{X}_{\cdot J}^\dagger \mathbf{X}\|_F}{\|\mathbf{X}\|_F} \quad (2)$$

and the stability of the interpolation map is determined by $\|\mathbf{X}_{\cdot J}^\dagger \mathbf{X}\|_\infty$. In the following, we will then focus on computing a subset J such that the error is small and the map is stable.

We will use much of the notation introduced above throughout the paper. When necessary, we will denote data matrices and errors corresponding to a training set by \mathbf{X}^{tr} and $e^{\text{tr}}(J)$ and the matrices and errors corresponding to a testing set by \mathbf{X}^{te} and $e^{\text{te}}(J)$. Note that

$$e^{\text{te}}(J) = \frac{\|\mathbf{X}^{\text{te}} - \mathbf{X}_{\cdot J}^{\text{te}} \mathbf{X}_{\cdot J}^{\text{tr}\dagger} \mathbf{X}^{\text{tr}}\|_F}{\|\mathbf{X}^{\text{te}}\|_F}, \quad (3)$$

i.e. the operator $\hat{\mathbf{T}}(J)$ is always determined by the training set. It is also common (see [8], [28], [30], [31]) to reduce the computational cost associated with finding J by applying the algorithm to an $r \times n$ matrix Ψ^{tr} which captures the dominant features of \mathbf{X}^{tr} for some $r \ll m$, e.g. to a matrix of singular vectors of \mathbf{X}^{tr} or a matrix given by random linear combinations of the rows of \mathbf{X}^{tr} . In this case, we define $\hat{\mathbf{T}}(J) = \Psi_{\cdot J}^{\text{tr}\dagger} \Psi^{\text{tr}}$.

It is now possible to define the linear sensor placement problem with cost constraints. Let $\boldsymbol{\eta}$ be the cost vector as described above and let s and b denote desired upper bounds on the stability of the map $\hat{\mathbf{T}}(J)$ and the budget, respectively. Then we may write the cost-constrained problem as

$$\hat{J} = \arg \min_J e(J) \text{ s.t. } \sum_{j \in J} \eta_j \leq b \text{ and } \|\hat{\mathbf{T}}(J)\|_{\infty, \text{vec}} \leq s, \quad (4)$$

where $\|\cdot\|_{\infty, \text{vec}}$ denotes the maximum absolute value over the entries of a matrix. Our algorithms will actually focus on the following relaxation of (4). Note that, for a given b , there exists a λ such that the problem

$$\hat{J} = \arg \min_J e(J) + \lambda \sum_{j \in J} \eta_j \text{ s.t. } \|\hat{\mathbf{T}}(J)\|_{\infty, \text{vec}} \leq s \quad (5)$$

and (4) have the same solution. Because we are often interested in the cost-error landscape, we seek the solution of (5) for a number of values of λ , so that we trace out a cost-error curve. We note that the main algorithm we present in Section III does not actually solve (5). Instead, we seek a greedy approximate solution which does not strictly enforce the stability constraint but uses a heuristic strategy to bias the sensors in favor of stability.

In the case that all entries of $\boldsymbol{\eta}$ are equal and positive, the constraint $\sum_{j \in J} \eta_j \leq b$ simplifies to the constraint $|J| \leq b/\eta_1$. This is closely related to the problem of optimally placing a specified number of sensors, a well-studied problem which we briefly review in the remainder of this section.

B. Theoretical results

As observed in [25], the strong rank revealing QR decomposition methods of [24] provide a polynomial time algorithm for computing a subset J such that the error $e(J)$ is near-optimally

small and the map $\hat{\mathbf{T}}(J)$ is near-optimally stable. The optimal performance is summarized in the following theorem.

Theorem 1: (adapted from [25]) Let $\mathbf{X} \in \mathbb{R}^{m \times n}$ and let $k \leq l = \min(m, n)$. Then, there exists a J such that $|J| = k$,

$$\|\mathbf{X} - \mathbf{X}_{\cdot J} \hat{\mathbf{T}}(J)\|_F \leq \sqrt{1 + k(l - k)} \sum_{j=k+1}^l \sigma_j(\mathbf{X}), \quad (6)$$

where $\sigma_j(\mathbf{X})$ denotes the j th singular value of \mathbf{X} , and

$$\|\hat{\mathbf{T}}(J)\|_F \leq \sqrt{k(n - k) + k}. \quad (7)$$

Remarkably, if we relax the bounds to

$$\|\mathbf{X} - \mathbf{X}_{\cdot J} \hat{\mathbf{T}}(J)\|_F \leq \sqrt{1 + lk(l - k)} \sum_{j=k+1}^l \sigma_j(\mathbf{X}), \quad (8)$$

and

$$\|\hat{\mathbf{T}}(J)\|_F \leq \sqrt{nk(n - k) + k}, \quad (9)$$

then there exist algorithms which compute such a J using, typically, $O(mnk)$ flops and at most $O(mnl)$ flops [24]. However, the standard QR algorithm with column pivoting tends to achieve similar bounds, with the worst case behavior limited to pathological examples (see the Kahan matrix example of [24]).

C. QR with column pivoting for sensor placement

Many of the standard implementations of routines for computing a QR decomposition are based on the application of Householder reflectors to triangularize a matrix [32]. Let a vector $\mathbf{v} \in \mathbb{R}^m$ be given. We can then define a Householder reflector [33] which maps \mathbf{v} to $\|\mathbf{v}\|_2 \mathbf{e}^1$, where \mathbf{e}^1 is the first standard basis vector in \mathbb{R}^m . Let $\sigma = \|\mathbf{v}\|_2$ and let v_1 denote the first entry of \mathbf{v} . Then, the matrix

$$\mathbf{H}(\mathbf{v}) := \mathbf{I} - \frac{(\mathbf{v} + \text{sign}(v_1)\sigma\mathbf{e}^1)(\mathbf{v} + \text{sign}(v_1)\sigma\mathbf{e}^1)^\top}{\sigma(\sigma + |v_1|)} \quad (10)$$

maps \mathbf{v} to $-\text{sign}(v_1)\sigma\mathbf{e}^1$. It is simple to verify that there exists a $\mathbf{u} \in \mathbb{R}^m$ of unit norm such that the map is given by $\mathbf{I} - 2\mathbf{u}\mathbf{u}^\top$, which is the standard form of a Householder reflector. This expression also makes it clear that $\mathbf{H}(\mathbf{v})$ is its own inverse.

Using the notation of [24], the standard QR decomposition algorithm with column pivoting applied to a matrix $\mathbf{X} \in \mathbb{R}^{m \times n}$ proceeds by iteratively defining an orthogonal matrix \mathbf{Q}^k and a permutation of the indices $J^k = \{j_1^k, \dots, j_n^k\}$ such that

$$\mathbf{X}\mathbf{P}(J^k) = \mathbf{Q}^k \begin{pmatrix} \mathbf{A}^k & \mathbf{B}^k \\ 0 & \mathbf{C}^k \end{pmatrix}, \quad (11)$$

where $\mathbf{A}^k \in \mathbb{R}^{k \times k}$ is upper triangular, $\mathbf{B}^k \in \mathbb{R}^{k \times (n-k)}$, $\mathbf{C}^k \in \mathbb{R}^{(m-k) \times (n-k)}$, and

$$\mathbf{P}(J^k) = \begin{pmatrix} \mathbf{e}^{j_1^k} & \mathbf{e}^{j_2^k} & \dots & \mathbf{e}^{j_n^k} \end{pmatrix}. \quad (12)$$

Let $J^0 = \{1, \dots, n\}$ and $\mathbf{Q}^0 = \mathbf{I}$. Denote the columns of \mathbf{C}^k by $\mathbf{c}^{k,i}$ for $i = 1, \dots, n - k$. To obtain the $k + 1$ st iterate from the k th, let $\mathbf{c}^{k,l}$ be the column of \mathbf{C}^k with the largest norm. We update the permutation indices to move this column to the front, i.e. $j_{k+1}^{k+1} = j_{k+1}^k$, $j_{k+l}^{k+1} = j_{k+l}^k$, and $j_i^{k+1} = j_i^k$ for all other i . If we update the orthogonal matrix \mathbf{Q}^k via

$$\mathbf{Q}^{k+1} = \mathbf{Q}^k \begin{pmatrix} \mathbf{I} & 0 \\ 0 & \mathbf{H}(\mathbf{c}^{k,l}) \end{pmatrix}, \quad (13)$$

then

$$\mathbf{X}\mathbf{P}(J^{k+1}) = \mathbf{Q}^k \begin{pmatrix} \mathbf{A}^{k+1} & \mathbf{B}^{k+1} \\ 0 & \mathbf{C}^{k+1} \end{pmatrix}, \quad (14)$$

where \mathbf{A}^{k+1} , \mathbf{B}^{k+1} and \mathbf{C}^{k+1} are of the correct form and $\mathbf{A}_{k+1,k+1}^{k+1} = \pm \|\mathbf{c}^{k,l}\|$.

The idea of using the column pivoted QR algorithm for sensor placement is that, for a given k , the first k pivots j_1^k, \dots, j_k^k should be a good choice of sensor locations. Let $J = \{j_1^k, \dots, j_k^k\}$. Then

$$\hat{\mathbf{T}}(J)\mathbf{P}(J^k) = \begin{pmatrix} \mathbf{I} & (\mathbf{A}^k)^{-1} \mathbf{B}^k \end{pmatrix} \quad (15)$$

and $e(J) = \|\mathbf{C}^k\|_F / \|\mathbf{X}\|_F$, so that both the stability of the map $\hat{\mathbf{T}}(J)$ and the error $e(J)$ are determined by the factors \mathbf{A}^k , \mathbf{B}^k , and \mathbf{C}^k .

Of course, for any permutation J^k of the indices, it is possible to construct a \mathbf{Q}^k using Householder reflectors such that \mathbf{A}^k , \mathbf{B}^k , and \mathbf{C}^k are of the correct form. In [24], it was shown that perfectly stable and highly accurate sensors, in the sense of Theorem 1, may be obtained by maximizing $|\det \mathbf{A}^k|$ over all possible permutations J^k . Because the \mathbf{A}^k are upper triangular, the column-pivoted QR procedure may be seen as a greedy method which approximates the optimal solution iteratively, updating J^{k+1} so that $|\det \mathbf{A}^{k+1}|$ is as large as possible with the first k entries of J^{k+1} fixed to be equal to the first k entries of J^k .

Remark 1: For the calculations in Sections IV and V, we computed $\hat{\mathbf{T}}(J)$ using the formula $\hat{\mathbf{T}}(J) = \mathbf{X}_J^\dagger \mathbf{X}$ and found that this worked well for our examples, though there may be an advantage to using a more numerically stable definition for $\hat{\mathbf{T}}(J)$, see (3.13) of [25].

D. Other work

The reduced order modeling community has long used a different method for selecting interpolation points of snapshot matrices: the discrete empirical interpolation method (DEIM) [28]. Let $\mathbf{v}^1, \dots, \mathbf{v}^k$ denote the first k right singular vectors of \mathbf{X} . The original DEIM procedure sets the interpolation points to be the pivots used when applying Gaussian elimination with partial pivoting to the matrix $(\mathbf{v}^1, \dots, \mathbf{v}^k)$. In [29], the Q-DEIM procedure was defined which instead chooses the interpolation points as the first k pivots of column-pivoted QR applied to the matrix $\mathbf{\Psi} = (\mathbf{v}^1, \dots, \mathbf{v}^k)^\top$. Q-DEIM has been observed to be generally more stable and accurate than DEIM [8], [29]. In this manuscript, we will refer to the methods which define $\mathbf{\Psi}$ in terms of singular vectors as DEIM-based.

Algorithm 1 QR pivoting with cost constraints.

Input: \mathbf{X} , k , η , γ

- 1: $m, n \leftarrow \text{size}(\mathbf{X})$
- 2: $\mathbf{R} \leftarrow \text{copy}(\mathbf{X})$
- 3: $\boldsymbol{\tau} \leftarrow \text{zeros}(\min(m, n), 1)$
- 4: $J \leftarrow 1 : n$
- 5: **for** $i = 1, \dots, k$ **do**
- 6: **for** $p = i, \dots, n$ **do**
- 7: $\nu_p \leftarrow \|\mathbf{R}_{i:m,p}\|_2 - \gamma \eta_{j_p}$
- 8: $l \leftarrow \text{index of the maximum of } \nu_{i:n}$
- 9: $\mathbf{v} \leftarrow \mathbf{R}_{i:m,i-1+l}$
- 10: $\text{swap}(\mathbf{R}_{i:m,i}, \mathbf{R}_{i:m,i-1+l})$
- 11: $\text{swap}(j_i, j_{i-1+l})$
- 12: $\sigma \leftarrow \|\mathbf{v}\|_2$
- 13: $\mathbf{w} \leftarrow (\mathbf{v} + \text{sign}(v_1)\sigma\mathbf{e}^1) / \sqrt{\sigma(\sigma + |v_1|)}$
- 14: $\mathbf{R}_{i:m,i:n} \leftarrow \mathbf{R}_{i:m,i:n} - \mathbf{w}\mathbf{w}^\top \mathbf{R}_{i:m,i:n}$
- 15: $\tau_i \leftarrow w_1$
- 16: $\mathbf{R}_{i+1:m,i} \leftarrow \mathbf{w}_{2:\text{end}}$

Output: \mathbf{R} , $\boldsymbol{\tau}$, J

For problems with many samples of data (large m), methods from randomized linear algebra may be used to decrease the computational cost of sensor placement [30], [31]. The randomized linear algebra approach is based on the fact that, with $r = k + t$ and the entries of $\mathbf{G} \in \mathbb{R}^{r \times m}$ drawn independently from a standard normal distribution, the row space of the matrix $\mathbf{\Psi} = \mathbf{G}\mathbf{X}$ closely approximates the space spanned by the first k right singular vectors of \mathbf{X} with a failure probability that decreases super-exponentially in t . For a matrix with fast singular value decay, typically t is taken to be 10 [31]. For data matrices, the singular values often decay slowly, so we take $r = 2k$ in our examples. We explore the performance of using true singular vectors, as in the DEIM framework, and using a randomized approach in Section IV.

III. ALGORITHM FOR SENSOR PLACEMENT UNDER COST CONSTRAINTS

In this section, we present pseudo-code for a greedy approach to the relaxed version of the cost-constrained sensor placement problem (5). The algorithm is based on the column-pivoted QR algorithm described in Section II-C, where the pivot column is chosen to balance the decrease in the error $e(J)$ with the increase in the total cost $\sum_{j \in J} \eta_j$. Within the pseudo-code, this balance is represented by the parameter γ (see Algorithm 1).

We note that, after iteration i of the outer for-loop in Algorithm 1, the matrix \mathbf{A}^i is stored in $\mathbf{R}_{1:i,1:i}$, \mathbf{B}^i is stored in $\mathbf{R}_{1:i,i+1:n}$, and \mathbf{C}^i is stored in $\mathbf{R}_{i+1:m,i+1:n}$. Therefore, when $\gamma = 0$, the pivot chosen in Algorithm 1 is the same as the pivot in column pivoted QR. At step $i + 1$ of the outer for-loop, the difference in the error, $e(J_{1:i}) - e(J_{1:i+1})$, is at least $\|\mathbf{v}\|_2 / (2\|\mathbf{X}\|_F \sqrt{n})$ (where \mathbf{v} is as in the pseudo-code). Therefore, a positive γ balances the decrease in the error, $e(J_{1:i}) - e(J_{1:i+1})$, with the cost of the pivot, $\eta_{j_{i+1}}$.

Remark 2: In Algorithm 1, the pivot chosen at step $i + 1$ of the outer for-loop does not necessarily correspond to

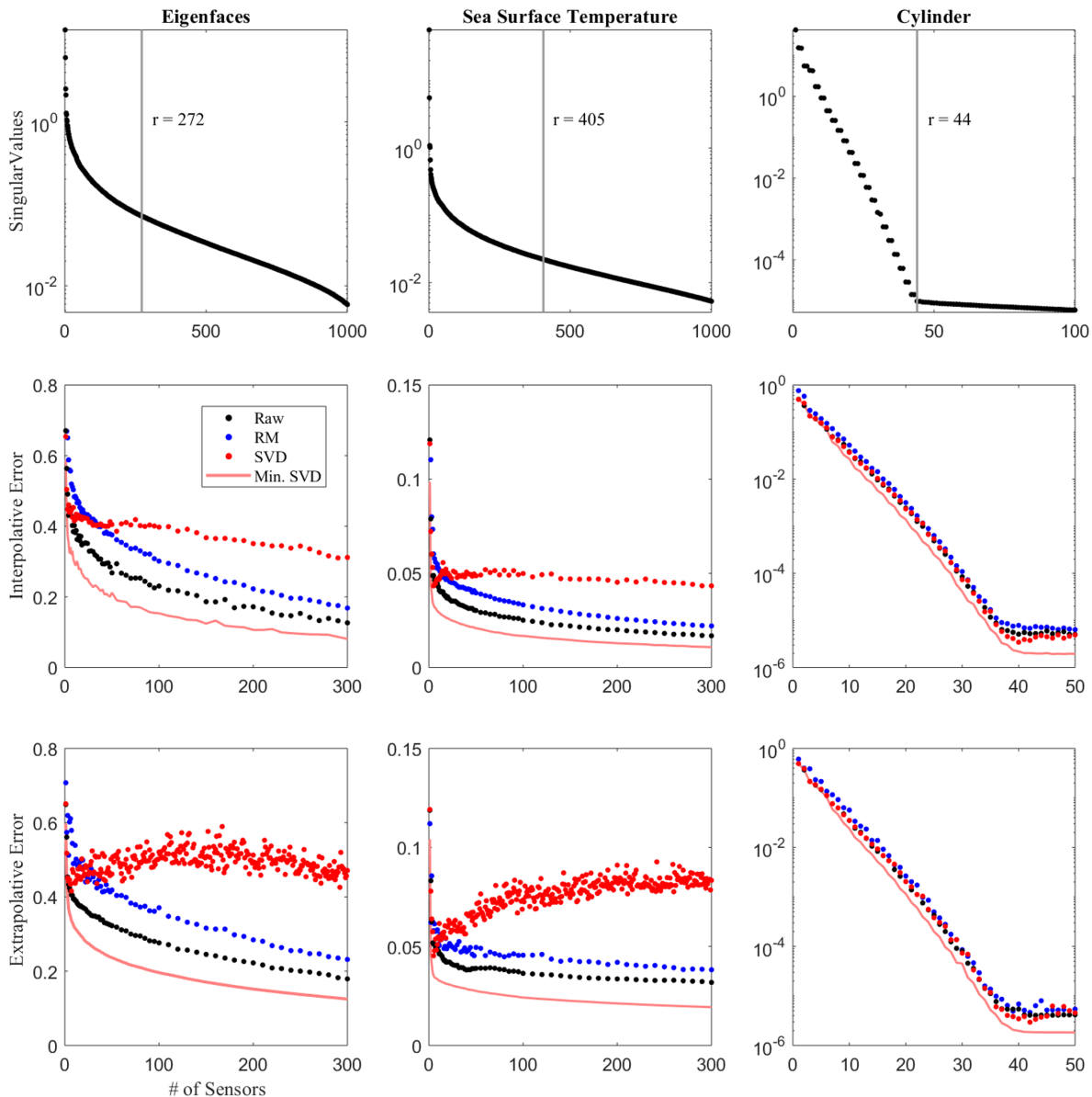


Fig. 1. Reconstruction error versus the number of sensors for the three data sets described in Section V, using p SVD modes, random linear combinations with $2p$ modes (abbreviated RM in the legend), and raw data. The top row shows a log plot of the normalized singular value spectrum, with the vertical gray line indicating the Gavish-Donoho cutoff r [34]. The remaining plots show the average reconstruction error given sensors placed using the three pre-processing methods discussed in the text. The first column provides eigenface results, the second gives sea surface temperature reconstruction errors, and the third shows reconstruction errors for the fluid flow behind a cylinder on a log scale. The middle row of the figure shows interpolative error, where the training set consists of a randomly-chosen subset of the data, while the bottom row gives the extrapolative data, which takes the first 80% of the parameter space. All plots also show a rough estimate of the minimum error at a given number of sensors (the solid red line), obtained by projecting the full image onto the SVD modes.

the natural greedy choice, i.e. the pivot which minimizes $e(J_{1:i+1}) + \gamma \sum_{j \in J_{1:i+1}} \eta_j$ with $J_{1:i}$ fixed. Such a pivot could be computed, though at greater cost than the present algorithm. Further, there is another reason to avoid such a strategy: it completely ignores the stability of the resulting map. By instead pivoting based on column size, we bias the algorithm toward choosing stable pivots while still incorporating some sense of the reduction in error.

Remark 3: We have also implemented an analogous algorithm based on Gaussian elimination with partial pivoting (in the spirit of the original DEIM algorithm). Because this approach performs significantly worse than the QR-based

algorithm, we omit the details.

IV. DATA, SINGULAR VECTORS, AND RANDOM PROJECTIONS

Before proceeding to the cost-constrained placement examples, we will first briefly discuss the question of data pre-processing for sensor placement. In the notation of Section II, pre-processing refers to the process of creating the matrix Ψ^{tr} from the training data \mathbf{X}^{tr} (we then apply the QR-based algorithm to Ψ^{tr}). When selecting p sensors, a common choice for the matrix Ψ^{tr} is to set it as the first p right singular

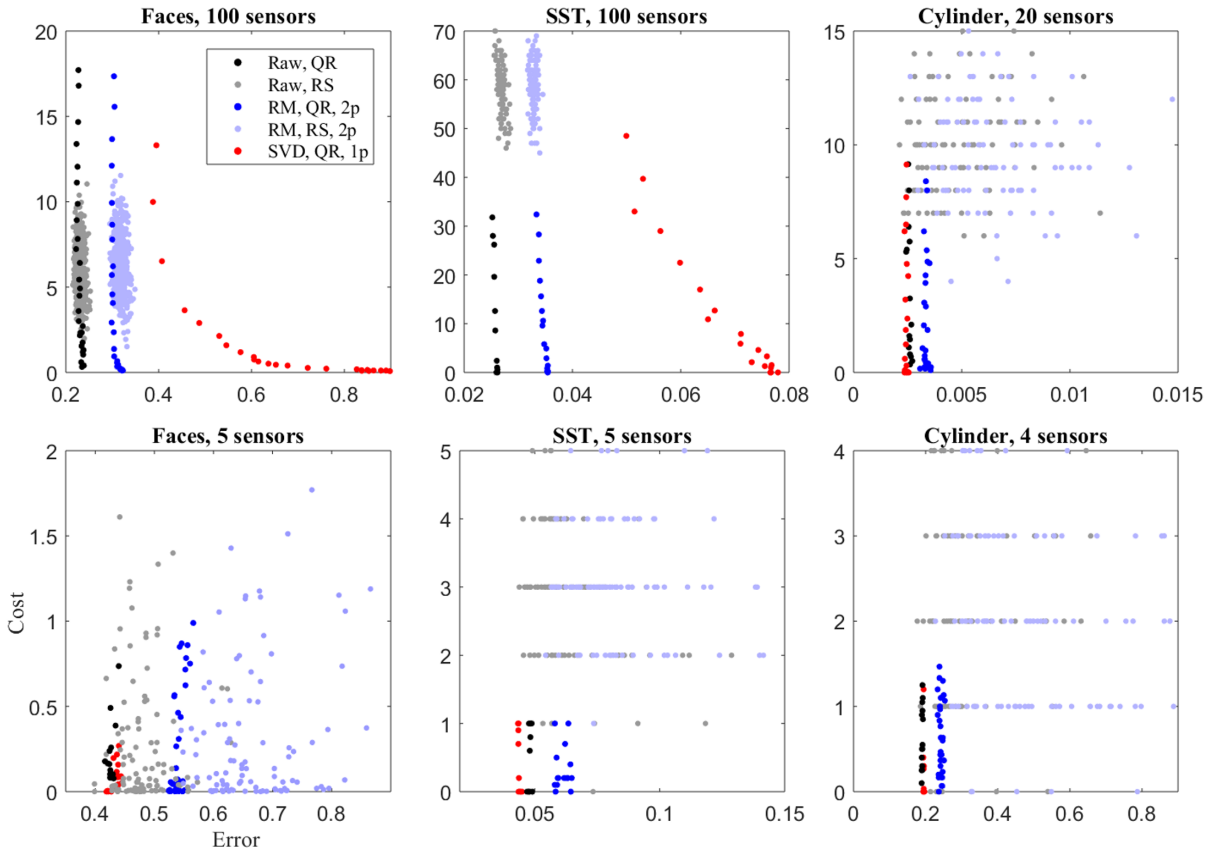


Fig. 2. A comparison of cost versus error results with several different pre-processing methods. The data sets and cost functions tested will be described in more detail in later sections. A Gaussian cost function is used for the eigenface example. The training set is interpolative, not extrapolative, with between 10 and 30 cross validations for each example. The methods used are as follows: First, performing the QR-based sensor placement algorithm directly on the raw data. Second, randomized linear combinations (abbreviated RM in the plot legend, for randomized modes) using $2p$ modes, where p is the number of sensors. Next, QR on p SVD modes. And finally, the sensor placement cost and reconstruction error are calculated from randomly-distributed sensors (abbreviated RS), with either the raw data or $2p$ randomized modes as a reconstruction basis. Randomized sensors using the SVD basis had significantly higher reconstruction errors than any other method, and the results are not shown here. The abbreviations in the legend are explained in Table I.

Color	Method	Description
●	Raw, QR	Performing the QR-based algorithm directly on the raw data.
●	Raw, RS	Randomly-placed sensors, using the raw data as a basis.
●	RM, QR, $2p$	QR on the randomized modes $\Psi = \mathbf{G}\mathbf{X}$, $\mathbf{G} \in \mathbb{R}^{2p \times m}$ a matrix with randomized entries.
●	RM, RS, $2p$	Using randomly-selected sensor locations, and $2p$ randomized modes as a basis.
●	SVD, QR, $1p$	QR on the first p SVD modes.

TABLE I

A BRIEF DESCRIPTION OF THE SENSOR PLACEMENT METHODS USED TO CREATE FIGURE 2, AND THE COLORS IN WHICH THEY ARE PLOTTED.

vectors of \mathbf{X}^{tr} [8], [28], [29]. Inspired by the randomized linear algebra community [30], [31], we also consider setting $\Psi^{tr} = \mathbf{G}\mathbf{X}^{tr}$, where the entries of $\mathbf{G} \in \mathbb{R}^{2p \times m}$ are drawn from a standard normal distribution, i.e. we set the rows of Ψ^{tr} to be random linear combinations of the rows of \mathbf{X}^{tr} . We also consider the performance when setting $\Psi^{tr} = \mathbf{X}^{tr}$, i.e. the performance without pre-processing. The number of singular

vectors or random linear combinations used is open-ended; we found that the choices above gave reasonably optimal performance for each pre-processing technique.

Our data sets are the Extended Yale Face Database B, the Optimally Interpolated Sea-Surface Temperature data set from NOAA, and simulation data for fluid flow behind a cylinder, all of which we will describe in more detail in the next section. For the face and sea surface temperature data, we consider two types of training sets: interpolative and extrapolative. By interpolative, we mean that we have sampled a subset of the data that draws from all regions of the parameter space. By extrapolative, we mean that we have purposefully missed data from a portion of the parameter space. For the faces data, that means we leave out all images belonging to 20% of the individuals. For the sea surface temperature data, that means we leave out samples from the last 20% of the dates. The data which is left out forms the testing set. Finding good sensor locations for the extrapolative training sets is a harder problem; the sensor locations must reasonably generalize to samples of data which may be unlike anything in the training set. We do not make this distinction for the fluid simulation data as it is much lower rank and periodic in time.

The top row of Figure 1 shows the spectrum of normalized

singular values for all three data sets. These plots include a gray line at the Gavish-Donoho [34] optimal hard-threshold cutoff, which is an estimate of the rank beyond which the SVD modes represent additive noise. It is apparent that the fluid flow data set is fundamentally different from the other two, having a sharp elbow at the cutoff, as opposed to a slow decay.

The remainder of Figure 1 plots the relative interpolation error (3) computed for the test set as a function of the number of sensors using each of the three methods for pre-processing (SVD modes, randomized modes, and the raw data) described above. The sea surface temperature and eigenface data sets both have an interesting feature not present in the fluid flow data: the error from the SVD basis has a local minimum at a very small number of modes – five for the temperature data and approximately ten for the eigenfaces. While the error for the interpolative training set begins to slowly decrease again as the number of sensors is increased, the performance for extrapolative data gets worse as more sensors are added, up until at least 150 sensors. This unexpected behavior reveals that, for systems with slow singular value decay, there is an overfitting problem when using SVD modes which occurs well before those modes correspond to additive sensor noise.

The reconstruction errors for sensors based on random linear combinations or the raw data do not have this behavior (except for a weak effect with extrapolative sea surface temperature data), nor do any of the cylinder trials. Indeed, the error for the random linear combinations and the raw data behaves as expected, decaying at a rate that follows the error obtained from projecting the test set onto the first p singular modes of the training set (this rough indicator of optimal behavior is plotted as a solid red line in the figure).

We make a few conclusions based on these pre-processing results. If the goal of pre-processing is to improve the quality of the sensors, then it appears that using no pre-processing is the preferred method, except when placing a very small number of sensors, where the SVD mode method displays an advantage. If the goal of the pre-processing is to reduce the size of the problem and speed up the optimization procedure, then it appears that using randomized linear combinations of the modes is preferable to using a limited number of SVD modes. (Note that these SVD modes would have to be computed with an accelerated procedure in order for using them to represent a speed-up over the QR-based sensor placement algorithm, again, with the caveat that SVD modes behave better for a small number of sensors.)

V. APPLICATIONS

When factoring in the effect of cost, we observe similar behavior to the cost-free case analyzed in the previous section. Figure 2 provides an overview of the performance for the various pre-processing methods, now with a non-zero cost associated to each location. In the plots, we generate several cost, error pairs for each pre-processing technique by varying the cost function weighting γ in the QR-based algorithm. We also plot the performance of randomly drawn sensors for the sake of comparison. All three data sets are considered, with

both a large and small number of sensors. See Table I for details on the figure labels.

For both the eigenface and sea surface temperature data sets, using the raw data at 100 sensors leads to the lowest error at a comparable cost, and randomized linear combinations with $2p$ modes gives the next lowest error, followed by SVD with p modes. At 5 sensors, the latter is reversed, with SVD performing comparably to or better than the raw data, as is the case with both trials for the fluid flow behind a cylinder. We observe that our QR-based method outperforms the best randomly chosen sensors when placing a large number at low cost, while choosing the best random sensors may offer an advantage when placing a small number (the randomly chosen sensors are more likely to contain the brute force answer in this case). We note that the randomized data performs worse than the raw data in all examples, but the behavior is consistent and may be worth the reduced computational cost in some applications.

In the remainder of this section, we more closely analyze the performance of the algorithm for each of our data sets. For brevity, we consistently use a randomized linear combination of data vectors for the pre-processing technique in these examples, noting that the behavior described above would be maintained if all techniques were tested.

A. Eigenfaces

The algorithms are first tested on the Extended Yale Face Database B, referred to here as the eigenface data set [35]–[38]. It comprises about 64 images each of 38 individuals under various lighting conditions. The images are downsized to 32×32 pixels.

Unless otherwise stated, the tests are conducted on an interpolative training set, by randomly selecting 80% of the images. The cost weighting factor γ is then progressively increased as the sensors are placed using the QR-based algorithm. Once the sensor locations are selected, the cost of the given array is calculated, and their average reconstruction accuracy is evaluated using the remaining 20% of the photographs. A 20-fold cross validation is performed.

Three cost functions are tested: 1) a Gaussian function, such that it is most expensive to place sensors in the center of the face, 2) a step function uniformly penalizing sensors in the middle ninth of the photographs, and 3) a step function penalizing the left third of the data set.

All three cost functions and a few corresponding sensor arrays are shown in Figure 3. These are the average locations over the twenty cross-validation runs, generated by the QR algorithm with 200 sensors, shown as a scatter plot on top of the dominant eigenface mode. Marker size and color indicate the frequency with which a sensor was placed at a given location. As expected, when the cost function weighting is increased, sensors are gradually pushed out of the regions of higher cost. This allows the total cost to be lowered at the expense of decreasing reconstruction accuracy, as demonstrated in the right-hand column of the figure, which plots cost and error on separate axes, as a function of γ . Note that γ is an arbitrary weighting, and the same value of γ can

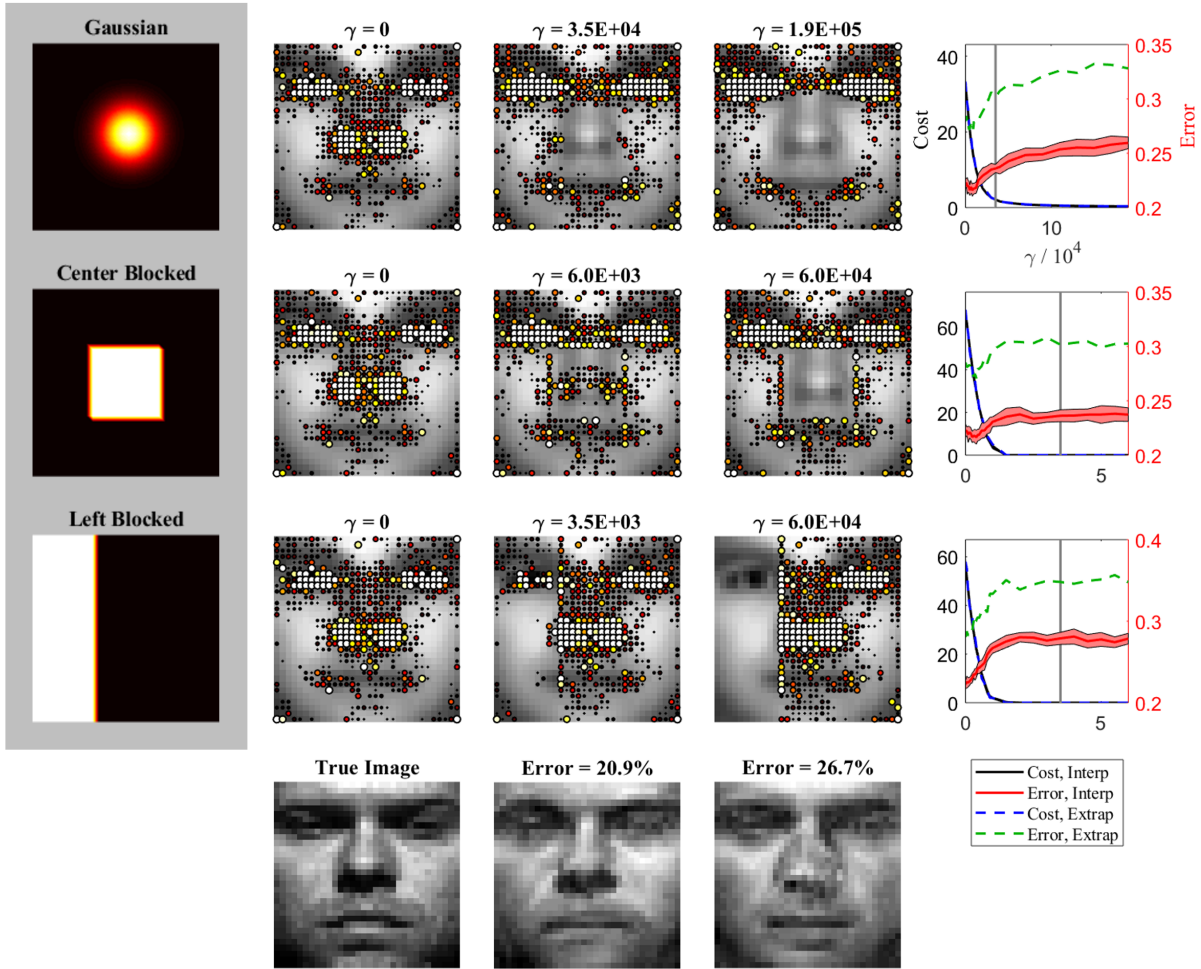


Fig. 3. Average sensor locations for eigenface reconstruction for three different cost functions. The cost functions are plotted in the left column, where white indicates regions of highest cost and black shows regions of zero cost. The three central columns show the locations of 200 sensors placed by the QR-based algorithm, averaged over 20 cross validations, for increasing values of the weighting factor γ . The final column plots cost and error against γ for each cost function, with bands indicating error bars. Both interpolation and extrapolation results are given. The vertical gray lines indicate the value of γ at which the sensors are plotted in the middle column. The bottom row shows typical example reconstructions of one of the photos, for reference.

have very different effects depending on the cost function. Extrapolative cost and error are shown in the same panel, where the extrapolative error is higher than the interpolative, at an identical cost. Additionally, the bottom row of the figure shows several reconstruction examples for one of the faces.

For many practical applications of these methods, the final goal will be to minimize reconstruction error given a predetermined budget. To that end, cost-error landscapes are constructed by calculating sensor array cost and reconstruction error for different numbers of sensors. The results are shown in Figure 4, which shows the landscapes for each cost function. These landscapes are plotted as a color map according to cost. Cost contours on this color map represent a hypothetical budget, so the optimum configuration for a given budget can be found by following the appropriate contour to the lowest possible error. Note that the upper edges of the contour plots indicate the minimum cost and maximum error for a given number of sensors, and the lower edges indicate the minimum error and maximum cost.

Cross sections of the cost landscapes as plots of cost versus

error are given in Figures 5 and 6. The former shows such cross sections for each of the three cost functions, using 200 sensors, and the latter shows cost versus error for a Gaussian cost function with 25, 100, 200, and 300 sensors.

B. Sea surface temperature

The next data set we consider is the NOAA_OISST_V2 mean sea surface temperature set [39]–[41], comprising weekly global sea surface temperature measurements between the years of 1990 and 2016. There are a total of 1400 snapshots on a 360×180 spatial grid. The QR-based algorithm is trained on 1100 randomly-selected snapshots and tested on the remaining 300. Ten cross validations are performed. The cost function used is a step function which penalizes placing sensors too far from shore, being zero for locations one and two pixels off land, and equal to one everywhere else.

Average sensor locations over ten cross validations with 200 sensors are shown in Figure 7, as a scatter plot where the size and color of a data point indicate the frequency with which a sensor was placed in that location (blue being

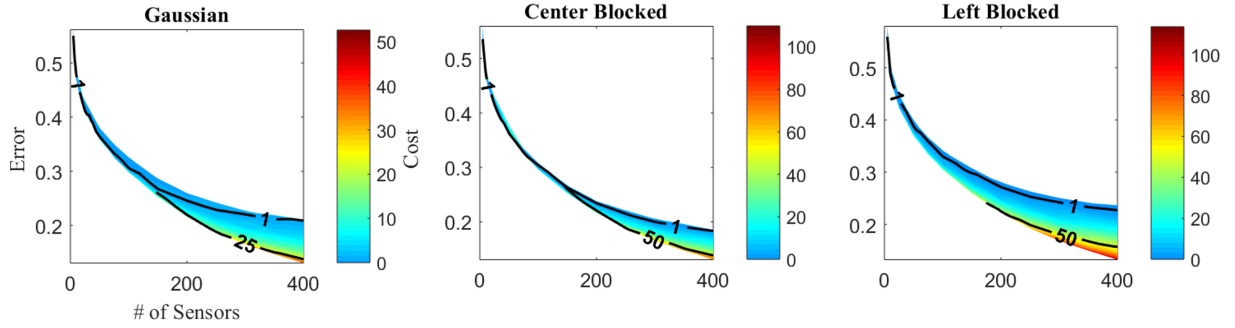


Fig. 4. The cost landscape for eigenface reconstruction for all three cost functions, with cost plotted as a two-dimensional color map against error and the number of sensors. Contours indicate lines of constant cost.

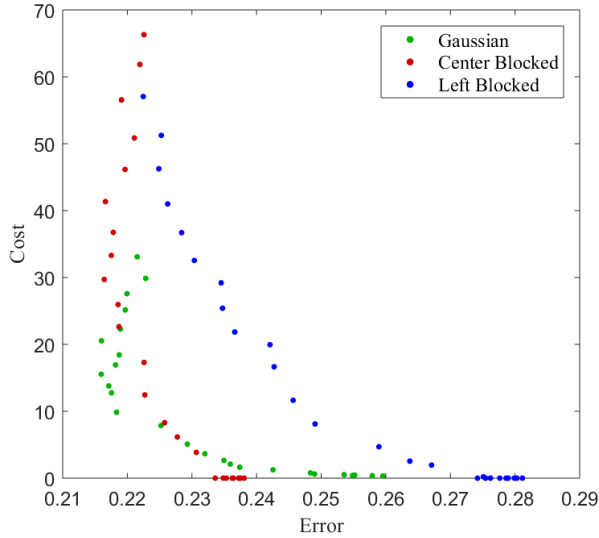


Fig. 5. Cost versus error for eigenface reconstruction with three different cost functions. Results are given for the case of 200 sensors.

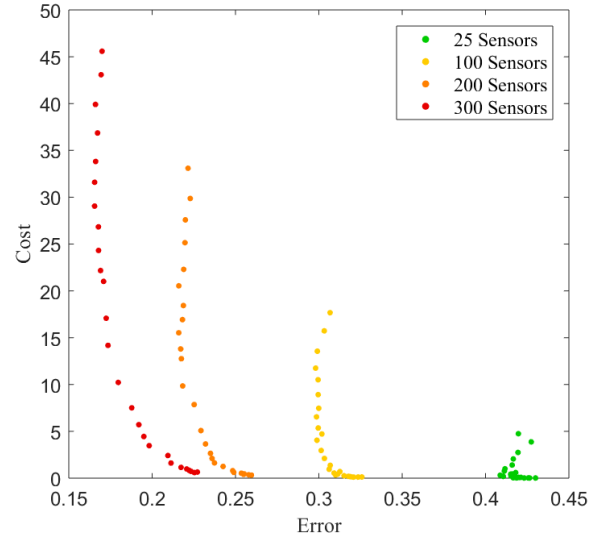


Fig. 6. Cost versus error for eigenface reconstruction with a Gaussian cost function, for several different numbers of sensors.

the least frequent, red being the most frequent). As the cost function weighting is increased, more sensors move within the unblocked regions offshore, until the cost reaches zero. Plots of cost and error as functions of γ are given in the fourth panel, and the bottom row shows two example reconstructions. As with the eigenfaces, the interpolative trial has a much lower error than the extrapolative trial. Notice that although the reconstruction error increases as cost decreases, here the error does not even reach 3%, even when the cost is zero.

The landscape of cost as a function of error and the number of sensors is shown in Figure 8, again visualized as a color map with contours of constant cost. Cross sections of cost versus error for 25, 100, 200, and 300 sensors are shown in Figure 10.

C. Fluid flow around a cylinder

As a final example, vortex shedding of a fluid flowing around a stationary cylinder is considered. This data set is low-rank, periodic, and vertically symmetric, making it a significant contrast to the previous two examples. The flow data were generated using the immersed boundary projection method [42], [43] to numerically simulate the Navier-Stokes

equations with Reynolds number 100. There are 151 snapshots in time, each on a 199×449 spatial grid.

The QR-based method is applied to the data set with a cost function that is uniformly one in the lower half of the domain and zero in the upper half. This allows the algorithm to take full advantage of the symmetry of the fluid flow, as can be seen in the figures. The data was generated using an interpolative training set of 120 randomly-selected snapshots; 30 cross validations were performed.

In Fig. 9, sensor locations for several values of the cost function weighting γ are shown. The locations were picked using the QR-based algorithm with 14 sensors, and are averaged over the 30 cross validations, then graphed as a scatter plot on top of an example fluid flow snapshot. The size and color of a data point indicate how frequently a sensor was placed at its location. As expected, when γ is increased, the sensors migrate until they occupy the upper half of the plane.

The fourth panel of the figure plots the cost and error on separate axes, as functions of γ . Because of the symmetry of the data set, the reconstruction error is essentially unchanged with γ , even as the cost goes to zero. Furthermore, because the flow is periodic, the extrapolative data performs slightly better than the interpolative data. The figure's bottom row shows

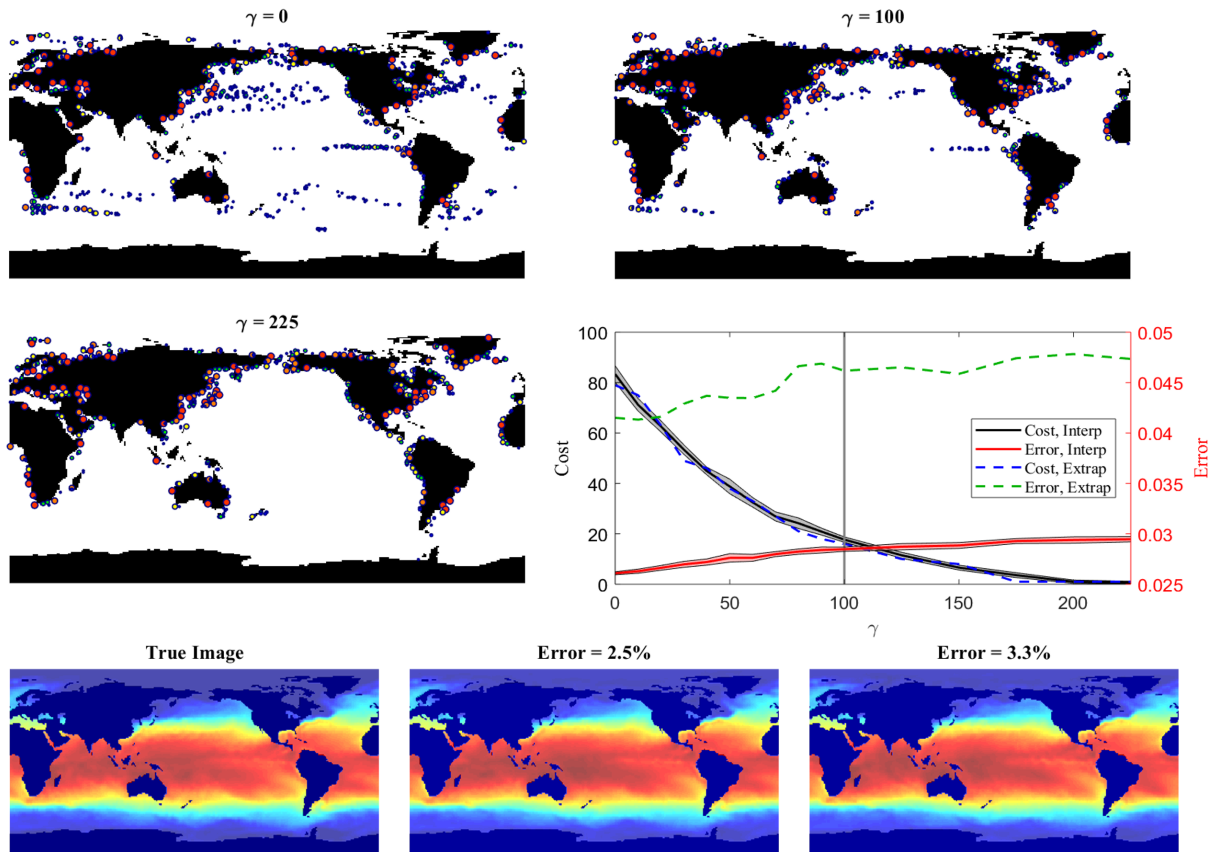


Fig. 7. Sensor locations for sea surface temperature reconstruction with 200 sensors. The cost function considered was a step function which was zero up to two pixels off land and equal to one everywhere else. Locations are shown for three different values of the weighting factor γ , and are averaged over ten cross validations. Size and color of a data point indicate the frequency with which a sensor was placed there. The fourth image plots cost and error against γ , for both interpolative and extrapolative data sets. The bottom row shows a comparison of an example temperature snapshot along with two reconstructions of it yielding two different accuracies.

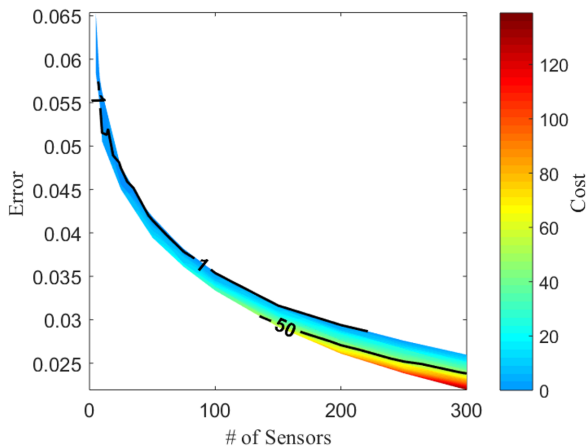


Fig. 8. The cost landscape for sea surface temperature reconstruction, plotted as a color map against error and the number of sensors. Contours show lines of constant cost.

example reconstructions of a snapshot.

The cost-error landscape is shown in Fig. 11. Notice that there is hardly any variation in the error, so rather than plotting cost as a color map, the error versus number of sensor curves

for $\gamma = 0$ (highest cost) and $\gamma = 15$ (lowest cost) are shown. These curves are essentially identical, further emphasizing that for this particular data set and cost function, the total cost can be lowered with no penalty to the error. Cost versus error plots are given in Fig. 12, which shows results for 4, 8, 12, and 20 sensors. Regardless of the number of sensors, these cross sections are essentially vertical lines, within the standard deviation of the error.

VI. CONCLUSION AND FUTURE DIRECTIONS

We have developed a QR-based greedy algorithm to place sensors for reconstruction with a cost constraint on sensor locations. This algorithm is tested on three different data sets, eigenfaces, weekly sea surface temperature data, and vortex shedding of a fluid flowing around a cylinder. In all cases, the method is demonstrated to be capable of lowering sensor cost at the expense of marginal increases in reconstruction error.

It is also shown that with or without the inclusion of a cost function, data sets with slow singular value decay have better results by pre-processing the data through a randomized linear combination of modes, rather than through SVD-based rank reduction. Random linear combinations lead to significantly lower reconstruction errors, except at a very low number of sensors.

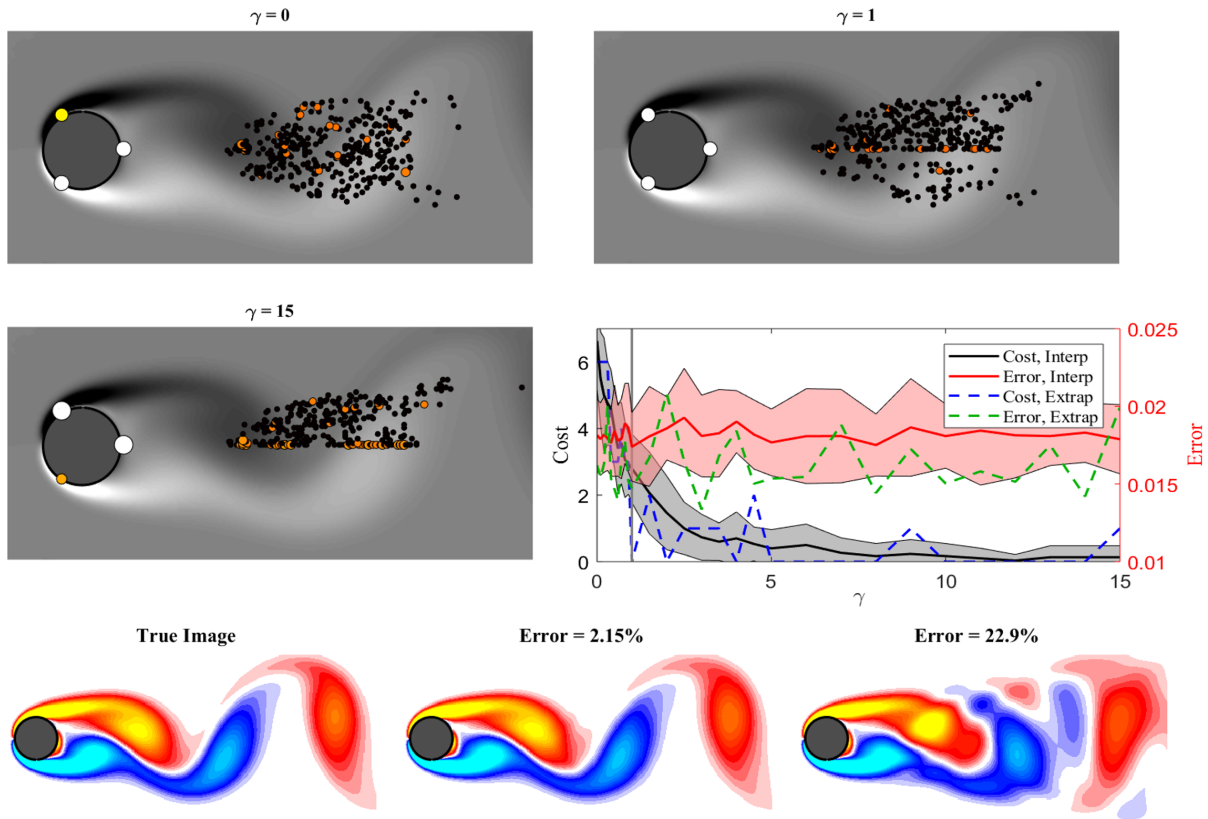


Fig. 9. Sensor locations and reconstructions of the flow behind a cylinder, obtained by the QR-based algorithm, using 14 sensors. The cost function was a step function blocking the lower half of the domain. The first three plots show the placements of the sensors averaged over 30 trials. The fourth shows cost and error plotted against γ , where the bands indicate error bars. The bottom row gives a comparison of the true image of a snapshot along with two different reconstructions.

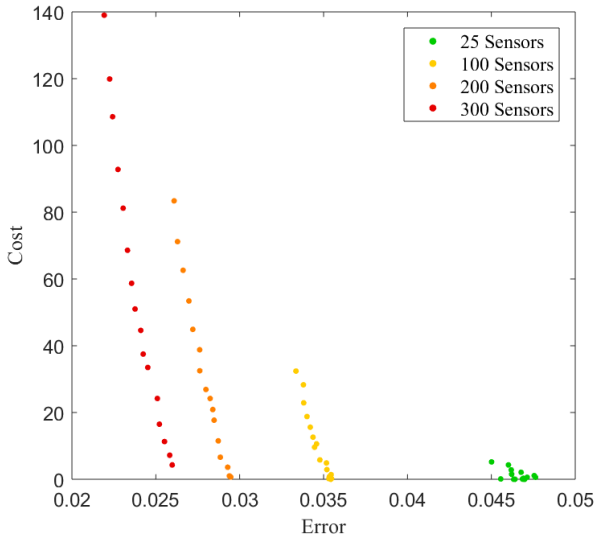


Fig. 10. Plots of cost versus error for sea surface temperature reconstruction, with varying numbers of sensors.

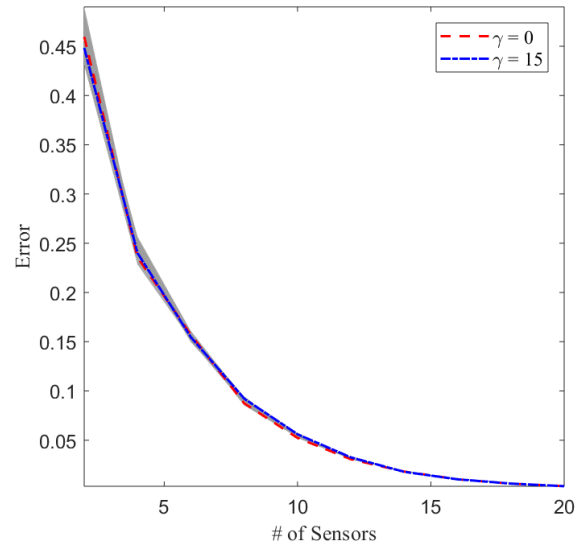


Fig. 11. The cost landscape for reconstruction of a fluid flow behind a cylinder. Instead of the color maps made for the previous two data sets, curves of error versus the number of sensors are shown for high and low values of γ . The gray band indicates the maximum variation in the error.

In fact, for these data sets with slow singular value decay, SVD modes behave in an unexpected way at a low number of modes. The reconstruction error decreases sharply, even surpassing the error obtained by using the full raw data in the case of sea surface temperatures, before increasing again as

more sensors are added. This suggests that the SVD is overfitting well before the Gavish-Donoho cutoff, an idea which warrants further exploration in future work. The results also

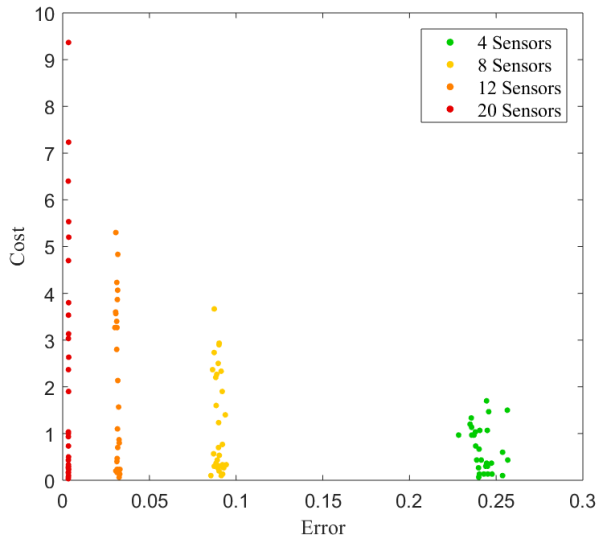


Fig. 12. Plots of cost versus error for cylinder flow reconstruction, with varying numbers of sensors.

imply that there may be some other pre-processing method which can take advantage of both the SVD behavior at a low number of sensors and the random linear combination or raw data behavior at a higher number of sensors. This will also be explored in the future.

In the meantime, the algorithm presented here provides a way to place sensors under a cost constraint, which could have applications in manufacturing, atmospheric sensing, fluid flow sensing, and many more fields. Specifically, the algorithm allows one to address three critical engineering design principles in regard to sensors placement: (i) For a fixed budget of sensors, where are the best measurement locations, (ii) What is the minimal number of sensors required to achieve a given reconstruction error, and (iii) How well can inaccessible regions be reconstructed in practice. Depending upon the application, one or all of these questions may be of central concern. The computationally tractable approach presented here provides a principled mathematical method for answering these questions.

ACKNOWLEDGMENT

T. Askham would like to thank Mark Tygert for useful discussions of the interpolative decomposition. T. Askham and J. N. Kutz acknowledge support from the Air Force Office of Scientific Research (FA9550-15-1-0385). S. L. Brunton acknowledges support from the Air Force Research Laboratory (FA8651-16-1-0003) and the Air Force Office of Scientific Research through the Young Investigator Program (FA9550-18-1-0200).

REFERENCES

- [1] J. Wright, A. Y. Yang, A. Ganesh, S. S. Sastry, and Y. Ma, "Robust face recognition via sparse representation," *IEEE transactions on pattern analysis and machine intelligence*, vol. 31, no. 2, pp. 210–227, 2009.
- [2] S. Joshi and S. Boyd, "Sensor selection via convex optimization," *IEEE Transactions on Signal Processing*, vol. 57, no. 2, pp. 451–462, 2009.
- [3] A. Krause, A. Singh, and C. Guestrin, "Near-optimal sensor placements in Gaussian processes: Theory, efficient algorithms and empirical studies," *Journal of Machine Learning Research*, vol. 9, no. Feb, pp. 235–284, 2008.
- [4] A. Krause, C. Guestrin, A. Gupta, and J. Kleinberg, "Near-optimal sensor placements: Maximizing information while minimizing communication cost," in *Proceedings of the 5th international conference on Information processing in sensor networks*. ACM, 2006, pp. 2–10.
- [5] Y. Zhang and J. G. Bellingham, "An efficient method of selecting ocean observing locations for capturing the leading modes and reconstructing the full field," *Journal of Geophysical Research: Oceans*, vol. 113, no. C4, 2008.
- [6] B. Yildirim, C. Chrysostomidis, and G. Karniadakis, "Efficient sensor placement for ocean measurements using low-dimensional concepts," *Ocean Modelling*, vol. 27, no. 3-4, pp. 160–173, 2009.
- [7] X. Yang, D. Venturi, C. Chen, C. Chrysostomidis, and G. E. Karniadakis, "EOF-based constrained sensor placement and field reconstruction from noisy ocean measurements: Application to Nantucket Sound," *Journal of Geophysical Research: Oceans*, vol. 115, no. C12, 2010.
- [8] K. Manohar, B. W. Brunton, J. N. Kutz, and S. L. Brunton, "Data-driven sparse sensor placement," *arXiv preprint arXiv:1701.07569*, 2017.
- [9] D. C. Kammer, "Sensor placement for on-orbit modal identification and correlation of large space structures," *Journal of Guidance, Control, and Dynamics*, vol. 14, no. 2, pp. 251–259, 1991.
- [10] S. Martı́nez and F. Bullo, "Optimal sensor placement and motion coordination for target tracking," *Automatica*, vol. 42, no. 4, pp. 661–668, 2006.
- [11] K. Lim, "Method for optimal actuator and sensor placement for large flexible structures," *Journal of Guidance, Control, and Dynamics*, vol. 15, no. 1, pp. 49–57, 1992.
- [12] X. Cheng, D.-Z. Du, L. Wang, and B. Xu, "Relay sensor placement in wireless sensor networks," *Wireless Networks*, vol. 14, no. 3, pp. 347–355, 2008.
- [13] E. J. Candès, J. Romberg, and T. Tao, "Robust uncertainty principles: Exact signal reconstruction from highly incomplete frequency information," *IEEE Transactions on information theory*, vol. 52, no. 2, pp. 489–509, 2006.
- [14] D. L. Donoho, "Compressed sensing," *IEEE Transactions on information theory*, vol. 52, no. 4, pp. 1289–1306, 2006.
- [15] E. J. Candès, J. K. Romberg, and T. Tao, "Stable signal recovery from incomplete and inaccurate measurements," *Communications on pure and applied mathematics*, vol. 59, no. 8, pp. 1207–1223, 2006.
- [16] E. J. Candès and T. Tao, "Near-optimal signal recovery from random projections: Universal encoding strategies?" *IEEE transactions on information theory*, vol. 52, no. 12, pp. 5406–5425, 2006.
- [17] R. G. Baraniuk, "Compressive sensing [lecture notes]," *IEEE signal processing magazine*, vol. 24, no. 4, pp. 118–121, 2007.
- [18] B. Moore, "Principal component analysis in linear systems: Controllability, observability, and model reduction," *IEEE transactions on automatic control*, vol. 26, no. 1, pp. 17–32, 1981.
- [19] K. Willcox and J. Peraire, "Balanced model reduction via the proper orthogonal decomposition," *AIAA journal*, vol. 40, no. 11, pp. 2323–2330, 2002.
- [20] C. W. Rowley, "Model reduction for fluids, using balanced proper orthogonal decomposition," in *Modeling And Computations In Dynamical Systems: In Commemoration of the 100th Anniversary of the Birth of John von Neumann*. World Scientific, 2006, pp. 301–317.
- [21] J.-N. Juang and R. S. Pappa, "An eigensystem realization algorithm for modal parameter identification and model reduction," *Journal of guidance, control, and dynamics*, vol. 8, no. 5, pp. 620–627, 1985.
- [22] R. Everson and L. Sirovich, "Karhunen–Loève procedure for gappy data," *JOSA A*, vol. 12, no. 8, pp. 1657–1664, 1995.
- [23] K. Willcox, "Unsteady flow sensing and estimation via the gappy proper orthogonal decomposition," *Computers & fluids*, vol. 35, no. 2, pp. 208–226, 2006.
- [24] M. Gu and S. C. Eisenstat, "Efficient algorithms for computing a strong rank-revealing QR factorization," *SIAM Journal on Scientific Computing*, vol. 17, no. 4, pp. 848–869, 1996.
- [25] H. Cheng, Z. Gimbutas, P.-G. Martinsson, and V. Rokhlin, "On the compression of low rank matrices," *SIAM Journal on Scientific Computing*, vol. 26, no. 4, pp. 1389–1404, 2005.
- [26] P.-G. Martinsson, V. Rokhlin, and M. Tygert, "On interpolation and integration in finite-dimensional spaces of bounded functions," *Communications in Applied Mathematics and Computational Science*, vol. 1, no. 1, pp. 133–142, 2007.

- [27] M. Barrault, Y. Maday, N. C. Nguyen, and A. T. Patera, “An ‘empirical interpolation’ method: application to efficient reduced-basis discretization of partial differential equations,” *Comptes Rendus Mathematique*, vol. 339, no. 9, pp. 667–672, 2004.
- [28] S. Chaturantabut and D. C. Sorensen, “Nonlinear model reduction via discrete empirical interpolation,” *SIAM Journal on Scientific Computing*, vol. 32, no. 5, pp. 2737–2764, 2010.
- [29] Z. Drmac and S. Gugercin, “A new selection operator for the discrete empirical interpolation method—improved a priori error bound and extensions,” *SIAM Journal on Scientific Computing*, vol. 38, no. 2, pp. A631–A648, 2016.
- [30] E. Liberty, F. Woolfe, P.-G. Martinsson, V. Rokhlin, and M. Tytgert, “Randomized algorithms for the low-rank approximation of matrices,” *Proceedings of the National Academy of Sciences*, vol. 104, no. 51, pp. 20 167–20 172, 2007.
- [31] N. Halko, P.-G. Martinsson, and J. A. Tropp, “Finding structure with randomness: Probabilistic algorithms for constructing approximate matrix decompositions,” *SIAM review*, vol. 53, no. 2, pp. 217–288, 2011.
- [32] P. Businger and G. H. Golub, “Linear least squares solutions by Householder transformations,” *Numerische Mathematik*, vol. 7, no. 3, pp. 269–276, 1965.
- [33] A. S. Householder, “Unitary triangularization of a nonsymmetric matrix,” *Journal of the ACM (JACM)*, vol. 5, no. 4, pp. 339–342, 1958.
- [34] M. Gavish and D. L. Donoho, “The optimal hard threshold for singular values is $4/\sqrt{3}$,” *IEEE Transactions on Information Theory*, vol. 60, no. 8, pp. 5040–5053, 2014.
- [35] D. Cai, X. He, Y. Hu, J. Han, and T. Huang, “Learning a spatially smooth subspace for face recognition,” in *Proc. IEEE Conf. Computer Vision and Pattern Recognition Machine Learning (CVPR’07)*, 2007.
- [36] D. Cai, X. He, and J. Han, “Spectral regression for efficient regularized subspace learning,” in *Proc. Int. Conf. Computer Vision (ICCV’07)*, 2007.
- [37] D. Cai, X. He, J. Han, and H.-J. Zhang, “Orthogonal Laplacianfaces for face recognition,” *IEEE Transactions on Image Processing*, vol. 15, no. 11, pp. 3608–3614, 2006.
- [38] X. He, S. Yan, Y. Hu, P. Niyogi, and H.-J. Zhang, “Face recognition using Laplacianfaces,” *IEEE Trans. Pattern Anal. Mach. Intelligence*, vol. 27, no. 3, pp. 328–340, 2005.
- [39] “NOAA optimal interpolation (OI) sea surface temperature (SST) v2.” [Online]. Available: <https://www.esrl.noaa.gov/psd/>
- [40] V. Banzon, T. M. Smith, T. M. Chin, C. Liu, and W. Hankins, “A long-term record of blended satellite and in situ sea-surface temperature for climate monitoring, modeling and environmental studies,” *Earth System Science Data*, vol. 8, no. 1, pp. 165–176, 2016. [Online]. Available: <http://www.earth-syst-sci-data.net/8/165/2016/>
- [41] R. W. Reynolds, T. M. Smith, C. Liu, D. B. Chelton, K. S. Casey, and M. G. Schlax, “Daily high-resolution-blended analyses for sea surface temperature,” *Journal of Climate*, vol. 20, no. 22, pp. 5473–5496, 2007.
- [42] K. Taira and T. Colonius, “The immersed boundary method: a projection approach,” *Journal of Computational Physics*, vol. 225, no. 2, pp. 2118–2137, 2007.
- [43] T. Colonius and K. Taira, “A fast immersed boundary method using a nullspace approach and multi-domain far-field boundary conditions,” *Computer Methods in Applied Mechanics and Engineering*, vol. 197, pp. 2131–2146, 2008.



Emily Clark received the B.S. degree in physics from Bates College, Lewiston, ME, in 2015. She is a Ph.D. student of physics at the University of Washington.



Travis Askham received the B.S. degree in applied mathematics and the M.A. degree in mathematics from the University of California, Los Angeles, Los Angeles, CA, in 2010 and the Ph.D. degree in mathematics from the Courant Institute of Mathematical Sciences at New York University, New York, NY, in 2016. He is a Research Associate of applied mathematics at the University of Washington.



Steven L. Brunton received the B.S. degree in mathematics with a minor in control and dynamical systems from the California Institute of Technology, Pasadena, CA, in 2006, and the Ph.D. degree in mechanical and aerospace engineering from Princeton University, Princeton, NJ, in 2012. He is an Assistant Professor of mechanical engineering and a data science fellow with the eScience institute at the University of Washington.



J. Nathan Kutz received the B.S. degrees in physics and mathematics from the University of Washington, Seattle, WA, in 1990, and the Ph.D. degree in applied mathematics from Northwestern University, Evanston, IL, in 1994. He is currently a Professor of applied mathematics, adjunct professor of physics and electrical engineering, and a senior data science fellow with the eScience institute at the University of Washington.